

# Effect of climb on dislocation mechanisms and creep rates in $\gamma'$ -strengthened Ni base superalloy single crystals: A discrete dislocation dynamics study

S.M. Hafez Haghighat<sup>a</sup>, G. Eggeler<sup>b</sup>, D. Raabe<sup>a,\*</sup>

<sup>a</sup> Max-Planck-Institut für Eisenforschung, Max-Planck-Str. 1, 40237 Düsseldorf, Germany

<sup>b</sup> Institut für Werkstoffe, Ruhr-Universität Bochum, Universitätsstr. 150, 44780 Bochum, Germany

Received 11 November 2012; received in revised form 28 February 2013; accepted 1 March 2013

Available online 29 March 2013

## Abstract

Creep of single-crystal superalloys is governed by dislocation glide, climb, reactions and annihilation. Discrete three-dimensional (3D) dislocation dynamics (DDD) simulations are used to study the evolution of the dislocation substructure in a  $\gamma/\gamma'$  microstructure of a single-crystal superalloy for different climb rates and loading conditions. A hybrid mobility law for glide and climb is used to map the interactions of dislocations with  $\gamma'$  cubes. The focus is on the early stages of creep, where dislocation plasticity is confined to narrow  $\gamma$  channels. With enhancing climb mobility, the creep strain increases, even if the applied resolved shear stress is below the critical stress required for squeezing dislocations into the  $\gamma$  channels. The simulated creep microstructure consists of long dislocations and a network near the corners of the  $\gamma'$  precipitate in the low-stress regime. In the high-stress regime, dislocations squeeze into the  $\gamma$  channels, where they deposit dislocation segments at the  $\gamma/\gamma'$  interfaces. These observations are in good agreement with experimentally observed dislocation structures that form during high-temperature and low-stress creep.

© 2013 Acta Materialia Inc. Published by Elsevier Ltd. All rights reserved.

**Keywords:** Superalloys; Dislocation dynamics; Simulation; Creep

## 1. Introduction

Single-crystal Ni base superalloys are used for gas turbine blades. During operation, the material undergoes creep deformation at temperatures far above half the melting point in kelvins. Creep is characterized by time-dependent plastic deformation. Creep rates show a strong non-linear dependence on stress (power law) and temperature (Arrhenius relation). The microstructure strongly determines the associated critical parameters. Therefore, controlling the creep rates requires a detailed understanding of the underlying microstructure–property relations, specifically of high-temperature dislocation plasticity and its effect on the power law and Arrhenius dependencies [1–8].

The microstructure of single-crystal Ni base superalloys consists of cubic  $\gamma'$  particles with L1<sub>2</sub> structure with

~0.5  $\mu\text{m}$  cube edge length separated by thin  $\gamma$  channels of a face-centered cubic Ni solid solution with ~0.1  $\mu\text{m}$  channel width. The channels and edges of the cuboidal precipitates are oriented along  $\langle 100 \rangle$  directions. After heat treatment, the  $\gamma$  channels contain a low dislocation density, and the  $\gamma'$  particles are free of dislocations [4–11].

The elementary mechanisms that govern creep deformation of single-crystal Ni base superalloys were extensively studied, identifying for instance the filling of channels by dislocations [9,12,13], the formation of dislocation networks around  $\gamma'$  cubes [14–16], misfit stresses [17–20] and the cutting of  $\gamma'$  particles by dislocations [21–28].

During the early stages of creep in the high-temperature and low-stress regime, the gradual filling of the  $\gamma$  channels by dislocations governs creep. During the later creep stages, the microstructure evolution is characterized by the rafting process [29,30] and the associated dislocation processes within this topologically modified microstructure [31]. Here, the focus on the low-stress and high-tempera-

\* Corresponding author. Tel.: +49 (0)211 6792 333.

E-mail address: [d.raabe@mpie.de](mailto:d.raabe@mpie.de) (D. Raabe).

ture creep regime where the controlling mechanisms during the early stage of creep are dislocation processes in the  $\gamma$  channels [9,13–21]. This work investigates two elementary dislocation processes in more detail, namely, glide and climb, in order to assess their relative importance with respect to the formation of the dislocation substructure in the channels and with respect to the accumulation of creep strain [22,32,33]. In a first-order approximation,  $\gamma'$  cubes are considered as inert and impenetrable elements of the microstructure that do not give rise to coherency stresses and which confine dislocation plasticity to the  $\gamma$  channels [9,13–21]. It is emphasized that in real systems misfit stresses occur [17–20,34], and they can actually be as high as 500 MPa. However, in the current model, the aim is to suppress the effects of misfit stresses in order to study solely the cooperation of climb and glide in the absence of other factors.

The simulation of single and collective dislocation behavior is essential for understanding the plastic deformation of Ni base single-crystal superalloys [39–43]. Among the different mean-field continuum-based crystal plasticity simulation techniques [42–47], discrete dislocation dynamics (DDD) models can provide insights specifically at the single-dislocation level. Corresponding simulations enable one to identify rate-limiting steps and provide information on the origin of dislocation patterns. Simulations also help to understand how strain accumulates and how this is related to dislocation mobilities, reactions, annihilation, climb and dynamic recovery. Such predictions provide a generic access to identify the rate-limiting relationships between microstructure, loading conditions, macroscopic creep rate and the resulting mechanical strength of the sample [48–77].

The DDD technique models the dynamics, reactions and far-field interactions of dislocations embedded in a linear continuum on the basis of the elasticity theory of dislocations [36,37,48–51,56–58]. DDD simulations have now reached a mature level such that complex dislocation mobility and interaction phenomena can be described in great detail [59–68]. The dislocation velocity is approximated by an overdamped viscous rate equation. The associated mobility contains glide, climb and cross-slip contributions [52,55]. The influence of cross-slip on the dislocation microstructure evolution has been investigated by the activation of this process in various DDD studies [51–69]. However, only a few studies addressed non-conservative effects in DDD simulations, for instance with the aim of understanding the effect of climb on the evolution of the dislocation substructure and on structure–property relations [68,73–75]. In these earlier studies, for instance, the propagation of single dislocations or loops due to climb forces and the microstructure evolution of dislocation ensembles in two-dimensions were investigated. A 3D analysis of dislocation climb in an array of multiple dislocations as a function of the dislocation character in two-phase systems has not yet been conducted.

DDD simulations have also been used to model dislocation interactions with the elastic fields surrounding obstacles [76,77], but only limited efforts were made to tackle dislocation plasticity in  $\gamma$  channels of  $\gamma/\gamma'$  microstructures [78,81]. Previous DDD studies on Ni base superalloys were concerned mainly with superdislocations in the  $\gamma'$  phase focusing on the role of cube size and shape,  $\gamma'$  volume fraction, temperature and anti-phase boundary energy [78–80]. The mechanical response of a single-crystal Ni base superalloy in the presence of a realistic dislocation density as a function of channel width,  $\gamma'$  particle shape and loading conditions has also been studied, taking into account the  $\gamma/\gamma'$  interface misfit stress [81,82]. All these studies addressed the uniaxial tensile creep deformation of Ni base superalloys, without considering dislocation climb.

The objective of this work is to use DDD simulations in conjunction with input parameters from experimental transmission electron microscopy (TEM) studies [22–33] with the goal of gaining insight into the relative contributions of glide and climb to dislocation motion in the  $\gamma$  channels of a  $\gamma/\gamma'$  microstructure of single-crystal superalloys. A parametric DDD study is performed on the importance of glide and climb processes [37,68,73], and the characteristic features of the dislocation substructures and reaction rates are related to the resulting creep rates. For this purpose, a modified DDD model is introduced that is capable of addressing creep deformation of single-crystal Ni base superalloy by employing a hybrid glide–climb mobility law. The simulation results are discussed in the light of previous experimental observations of individual dislocation mechanisms.

## 2. Simulation technique

### 2.1. DDD simulation methodology

The ParaDiS code [83] developed at Lawrence Livermore National Laboratory is used for the DDD simulations. In this approach, the dynamics is based on dislocation line decomposition and a nodal formulation of the dislocation segments. The dislocation lines are discretized to a maximum length of 12.5 nm. Each segment is characterized by its Burgers vector, glide plane normal and line direction. The force on a dislocation node is calculated by the summation of all Peach–Koehler (PK) forces resulting from an external applied stress, the local line tension and the stress field due to other dislocation segments. The segment positions are defined by calculating the speed of the node and the local events occurring during the displacement. These can include direct annihilation, junction formation and cross-slip, but must also account for the interaction with other elements of the microstructure such as, in the present case, the  $\gamma'$  cubes.

DDD simulations are conducted for two different types of setup. The first is a cubic box 500 nm in length, oriented along the crystallographic  $\langle 100 \rangle$  directions. It contains in its center a cubic  $\gamma'$  particle 420 nm in length, also oriented

in  $\langle 100 \rangle$  directions. This corresponds to a single-crystal Ni base superalloy of 59%  $\gamma'$  volume fraction with a channel width of  $w = 80$  nm. Creep deformation is modeled by applying constant tensile stresses of various magnitudes, i.e., 150, 250 and 350 MPa, along the  $[100]$  direction. This loading condition leads to a Schmid factor of 0.408 on the eight active  $\langle 110 \rangle \{111\}$  slip systems. Periodic boundary conditions (PBC) are applied along the three  $\langle 100 \rangle$  directions of the simulation box in order to account for the bulk microstructure that is characterized by the 3D periodic arrangement of the  $\gamma'$  cubes. As mentioned above, the  $\gamma/\gamma'$  interfaces are here assumed to be impenetrable boundaries according to experimental observations during the early stages of creep [1–4]. It should be noted that artifacts related to self-annihilation due to the use of PBC (as reported in Ref. [84]) can be neglected here, owing to the presence of a non-zero climb mobility. This effect avoids self-annihilation of the dislocations during propagation in a slip plane. However, it is important to account for the effect of short-range self-interaction of the dislocations resulting from the use of PBC. For a second set of simulations, therefore, a sample box 1000 nm in length including eight iso-shaped  $\gamma'$  cubes was used. The results were compared with those obtained for the single-particle simulation setup. The  $\gamma/\gamma'$  interface is treated as a rigid impenetrable and immobile boundary. Rafting is neglected.

TEM observations conducted on annealed Ni base superalloys reveal straight dislocations in the  $\gamma$  channels [9–11]. When exposed to creep, these dislocations evolve into microstructures that are characterized by the squeezing of dislocations into the  $\gamma$  channel and by their subsequent sliding along the  $\gamma/\gamma'$  interfaces by a climb-assisted mechanism. Therefore, the DDD simulations start out with a homogeneous distribution of mixed character 710-nm-long dislocations associated with 12 slip systems. These dislocations are straight and not pinned. Therefore, they are able to move freely and interact with the  $\gamma'$  cubes by the glide–climb mechanism and/or by squeezing into the  $\gamma$  channels. The average starting dislocation density over the entire simulation box is  $\sim 6.7 \times 10^{13} \text{ m}^{-2}$ . Isotropic elastic properties with a shear modulus of  $\mu = 37$  GPa and a Poisson ratio of  $\nu = 0.37$  are assumed. The lattice parameter of Ni alloy is taken as  $a = 0.36$  nm, implying a Burgers vector of  $b = 0.25$  nm.

## 2.2. Glide–climb mobility law

A coupled glide–climb mobility law is employed for the dislocation segments on the basis of the suggested interaction mechanism between the dislocations and the  $\gamma'$  cubes [22,32,33]. The experiments revealed that creep in these materials is strongly controlled by climb of the dislocations that are deposited at the  $\gamma/\gamma'$  interfaces. It is suggested that, in the early stages of creep, the  $1/2a_0\langle 110 \rangle \{111\}$  dislocations enter the thin  $\gamma$  channels by a squeezing mechanism leading to the deposition of a dipole consisting of two either  $60^\circ$  mixed or screw dislocations of opposite sign on

the two  $\gamma/\gamma'$  interfaces. Interface dislocations from vertical channels may then climb towards the channel crossings at the corners of the  $\gamma'$  cubes, where they can interact with dislocations from horizontal  $\gamma$  channels. This mechanism was suggested as the governing dynamic recovery process before rafting starts [22,32–38]. Fig. 1 shows the schematic trajectory of the nodal displacement of a dislocation in the vicinity of the  $\gamma'$  particle.

To implement this mechanism in the DDD simulations, a hybrid glide and climb mobility law is introduced for dislocation motion in the  $\gamma$  phase. In the current DDD model, dislocations cannot cross the  $\gamma/\gamma'$  interface. Instead, leading screw segments that move through the  $\gamma$  channels deposit  $60^\circ$  dislocations along the interface, which can move relative to the interface either by climb or by a coupled glide–plus–climb mechanism. In order to study the specific effect of climb on this high-temperature creep scenario without interfering with other effects of the Ni base superalloy, it is here assumed that the interface is a fixed rigid boundary without misfit stresses. In a recent work, Huang et al. [82] have shown, using DDD simulation, that the influence of the misfit stress in the stress–strain response of Ni base superalloys is negligible. However, in their DDD study, no climb processes had been involved.

In the ParaDiS code the applied PK force  $\mathbf{F}$  acting jointly from different sources on a dislocation segment is related to the segment velocity  $\mathbf{V}$  by

$$\mathbf{F} = \mathbf{B}\mathbf{V} \quad (1)$$

where  $\mathbf{B}$  is the drag tensor acting on the segment. Here, a hybrid mobility law is defined in the calculation of drag tensor to treat the interaction of moving dislocations with the  $\gamma'$  cube, as schematically illustrated in Fig. 1. Two drag tensors are calculated for all dislocation nodes according to

$$\mathbf{B}_{gc} = B_g(\mathbf{m} \otimes \mathbf{m}) + B_c(\mathbf{n} \otimes \mathbf{n}) + B_l(\mathbf{t} \otimes \mathbf{t})B_{gc}, \quad \mathbf{m} = \mathbf{n} \times \mathbf{t} \quad (2)$$

$$\mathbf{B}_{oc} = B_c(\mathbf{n} \otimes \mathbf{n}) \quad (3)$$

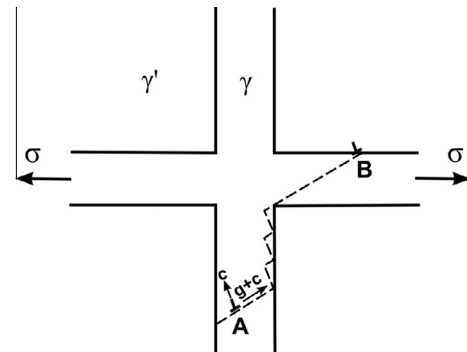


Fig. 1. Trajectory of the movement of a typical mixed  $1/2a_0\langle 110 \rangle \{111\}$  dislocation from position A to position B by either glide–climb or climb motion along the  $\gamma/\gamma'$  interface. Finally, the dislocation is released from the corner of the  $\gamma'$  particle, where it then penetrates the  $\gamma$  channel parallel to the applied stress direction.

where  $B_{gc}$  and  $B_{oc}$  are segment drag tensors for coupled glide–climb mobility (Eq. (2)) and for pure climb mobility (Eq. (3)), respectively. In these equations,  $\mathbf{n}$  is the glide plane normal unity vector,  $\mathbf{t}$  is the dislocation segment line direction unity vector,  $B_g$ ,  $B_c$  and  $B_l$  are the drag coefficients in glide, climb and line direction, respectively, and  $\otimes$  denotes the dyadic product.  $B_l$  is a drag coefficient to equilibrate the segment size distribution along the dislocation line. Its value is much smaller than that of  $B_g$  and  $B_c$ , so that it does not affect the kinetics of the dislocation line [83]. The glide and climb drag coefficients are obtained by

$$B_g = [B_{eg}^{-2} \|\mathbf{b} \times \mathbf{t}\|^2 + B_{sg}^{-2} (\mathbf{b} \cdot \mathbf{t})^2]^{-1/2} \quad (4)$$

$$B_c = B_{ec} \|\mathbf{b} \times \mathbf{t}\| \quad (5)$$

where  $\mathbf{b}$  is the normalized Burgers vector, and  $B_{eg}$ ,  $B_{sg}$  and  $B_{ec}$  are the drag coefficients of pure edge glide, pure screw glide and pure edge climb, respectively. They are related to the segment mobility via  $M_x = 1/B_x$ , which is used as the input parameter in the calculations. Eqs. (4) and (5) are used to interpolate the drag coefficient from the edge glide mobility to the screw glide mobility and from the maximum climb mobility of the edge segments to the quasi-zero climb mobility of the screw segments. The latter value is of course irrelevant, since screw components do not require non-conservative motion, but can rather glide conservatively in any direction prescribed by the force vector. The resulting drag coefficients of dislocation glide and climb, obtained from Eqs. (4) and (5), for the specific cases of the edge, 60° mixed and screw dislocation segments are given in Table 1. Different values for the effective climb mobilities,  $M_c$ , are used in the DDD simulations to introduce the influence of different temperatures. The glide mobility values of both the edge and screw dislocation segments are set to  $1 \text{ (Pa s)}^{-1}$  and only the climb mobilities of the edge components of each segment increase with increasing temperature. The corresponding changes in the climb mobility are realized by modifying the ratio of the glide-to-climb mobility coefficients according to  $M_g/M_c = 10, 100$  and  $1000$ . These climb mobility changes relate to temperature variations of a few tens of degrees kelvin within the range 900–1000 °C. In this regime,  $B$  increases with temperature; however, its changes are assumed to be insignificant. In addition, at high applied stresses and with increasing stress, the dislocation speed falls below values given by Eq. (1) and approaches the transverse sound velocity in the material [85]. The applied stress in the present simulations is far below the threshold stress

value that would be required to accelerate the dislocation speed towards the sound velocity, where the force–velocity relation of dislocations deviates from its linear form. It should be noted that the high dislocation speeds (and the associated high strain rates) in the current DDD simulations are due to the low drag coefficient. The low drag force is assumed in order to enable reasonable simulation times. A constant glide drag coefficient is assumed throughout the current calculations.

Applying these mobility values ( $1 \text{ (Pa s)}^{-1}$ ) in the DDD simulations will result in relatively high strain rates and relatively small creep times compared with real creep tests [1–10]. This is necessary, however, to run the simulations at reasonable computation times. It should be noted though that the dislocation mobility and their interactions are based on elasticity theory in DDD simulation, therefore, the effects are only weakly temperature dependent. Changing the strain rate would alter the predictions only when effects with larger thermal activation barriers were to be directly included. In the current DDD simulations, however, temperature is introduced only through an effective drag coefficient and the relative variation in the glide-to-climb mobility ratio as a function of temperature. Consequently, the high strain rates obtained in the calculations do not alter the final conclusions, since they depend only on the ratio of the glide/climb mobility values (mimicking temperature). Also, the time step controller, the so-called trapezoid time integrator [83] that has been implemented in the ParaDiS code, enables us to adjust the simulation time step without overlooking any topological event.

With the two drag tensors having been defined in Eqs. (2) and (3), the following algorithm is used for applying one of the tensors to the calculation of the displacement of a specific node in a DDD simulation step. Eq. (1) is used to calculate the velocity and new position of the node.

- The new position of a node is calculated using  $B_{gc}$ .
- If the new position of the node remains inside the  $\gamma$  phase, the displacement is accepted.
- Otherwise, if the segment leaves the channel with its new position, the new coordinate of the node is instead calculated using a climb step predicted by applying  $B_{oc}$ .
- If the new position of the node is inside the  $\gamma$  phase channel, the displacement is accepted.
- Otherwise, if the segment does not remain inside the  $\gamma$  phase, the displacement of the node is rejected in the current DDD simulation step.

This mobility algorithm prohibits dislocations from crossing from the  $\gamma$  phase into the  $\gamma'$  particle and simultaneously enables them to move along the  $\gamma/\gamma'$  interfaces if the resulting climb vector remains inside the  $\gamma$  phase. The next section discusses in more detail how this mobility law works regarding the interaction of a  $1/2a_0[011](1-11)$  dislocation that is located inside a  $\gamma$  channel with a  $\gamma'$  cube.

Table 1  
Glide and climb drag coefficients of a dislocation segment for the specific cases of the edge, 60° mixed and screw dislocation segments, respectively, obtained from Eqs. (4) and (5).

Dislocation character	$B_g$	$B_c$
Edge	$B_{eg}$	$B_{ec}$
60° mixed	$B_{eg}$	$B_{ec} \sin 60^\circ$
Screw	$B_{sg} = B_{eg}$	0



### 3. DDD simulation results

#### 3.1. Single-dislocation glide–climb mobility

Snapshots of predicted interaction scenarios between a  $1/2a_0[011](1-11)$  mixed  $60^\circ$  dislocation oriented in the  $[10-1]$  direction and a  $\gamma'$  particle with  $M_g/M_c = 10$  mobility ratio are shown in Fig. 2. Tensile loading of 150 MPa is applied along the  $y = [010]$  direction. The images reveal that, when the dislocation approaches the  $\gamma'$  precipitate, it starts to squeeze into the neighboring  $\gamma$  channels. Simultaneously, the segments that are hindered in their motion by the  $\gamma'$  cube, start to move along the  $\gamma/\gamma'$  interface fully in line with the mechanism shown in Fig. 1. The dislocation is then released from the top-right corner of the  $\gamma'$  cube, depositing the two dislocations of opposite sign along the two  $\gamma/\gamma'$  interfaces perpendicular to the  $x$  and  $z$  directions. However, it appears that, with further mechanical loading, the released segments are not able to penetrate the next  $\gamma$  channel through the PBC (Fig. 2).

Plastic strains and dislocation densities resulting from this type of interaction as a function of simulation time

are shown in Fig. 3. Three different stages of the interaction are established; the region denoted by (A) relates to the linear variations in strain and dislocation density in a regime where dislocations experience little glide resistance before approaching the  $\gamma'$  cubes (free glide regime). Region (B) marks the regime that is characterized by the interaction of the dislocation with the  $\gamma'$  cube using the coupled glide–climb motion towards the precipitate corner and the squeezing of the two dislocation arms into the neighboring  $\gamma$  channels (interaction regime). Region (C) represents the final release process of the dislocation from the corner of the particle by the annihilation of the released segments (relaxation regime).

The dislocation density remains constant in regime (A). When the dislocation reaches the  $\gamma/\gamma'$  interface (B) the lateral dislocation arms squeeze into the neighboring channels, creating new dislocation segments. The dislocation density further increases in this regime as a result of the expansion of the dislocation along the  $\gamma/\gamma'$  interface. Serrations in the dislocation density curve observed in region (B) are due to the stair-like movement of the dislocation segments along the  $\gamma/\gamma'$  interface, and the associated switching

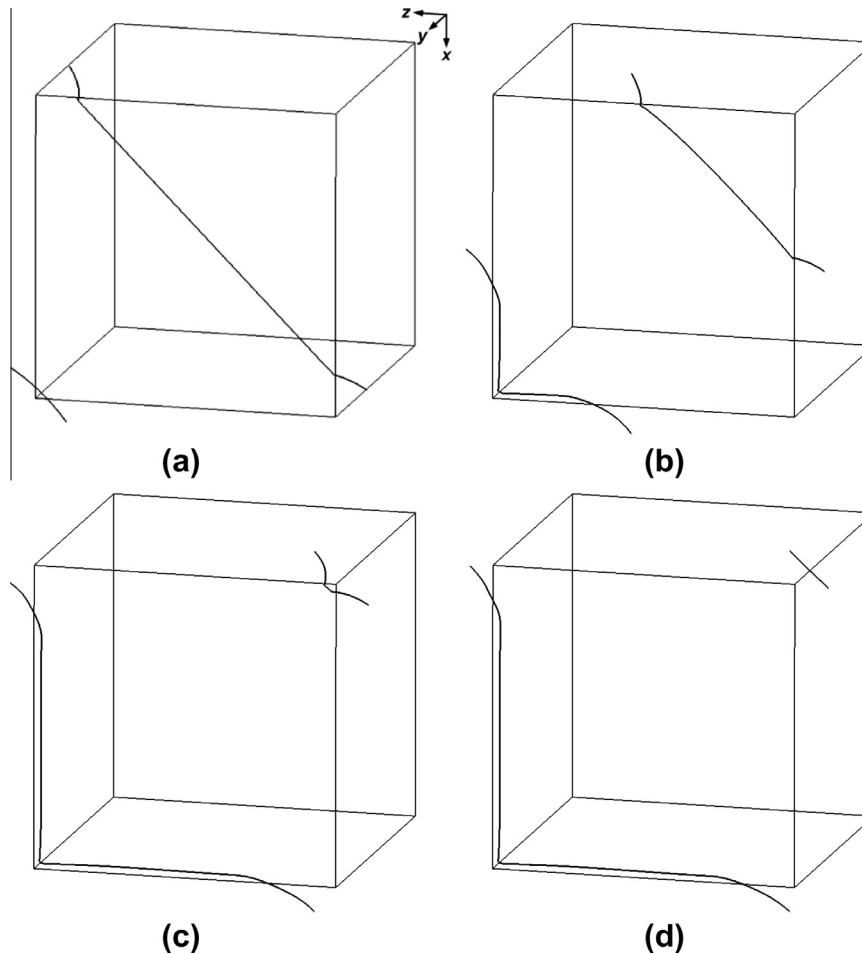


Fig. 2. Snapshots of the interaction between a  $1/2a_0[011](1-11)$   $60^\circ$  mixed dislocation oriented along the  $[10-1]$  direction and a  $\gamma'$  cube particle in a single-crystal Ni base superalloy loaded at 150 MPa tensile stress along the  $y$  direction. The sequence of this interaction consists of (a) the squeezing of the lateral dislocation segments into the  $\gamma$  channel shortly after approaching the  $\gamma'$  cube, (b) dislocation cubic slip with glide–climb mobility in the  $[-10-1]$  direction towards the top-right corner of the  $\gamma'$  cube, dislocation shortly (c) before and (d) after its release from the corner of the  $\gamma'$  cube.

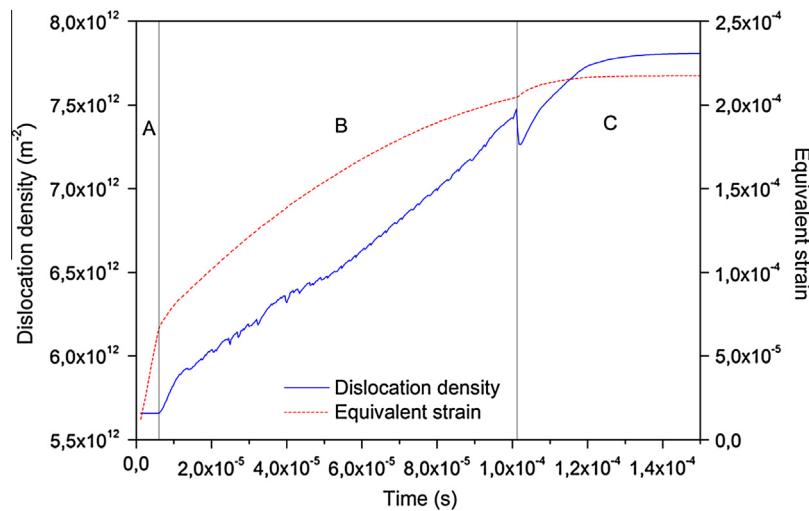


Fig. 3. Dislocation density and equivalent strain as a function of simulation time for the interaction of a  $1/2a_0[011](1-11)$  mixed  $60^\circ$  dislocation with a 420 nm  $\gamma'$  cube shown in Fig. 2. The interactions comprise three stages, namely, (A) the low-resistance glide of the dislocation before it approaches the particle; (B) the interaction of the dislocation with the  $\gamma'$  cube by coupled glide–climb motion towards the particle corner and the squeezing of the lateral segments of the dislocation into the  $\gamma$  channels, and (C) the final release of the dislocation from the  $\gamma'$  cube corner with the annihilation of the released segments.

between microscopic glide and coupled glide–climb steps. The dislocation line is not necessarily straight, owing to the hybrid mobility law employed. Jogs frequently form and annihilate all along the dislocation line. This rationalizes the ups and downs in the evolution of the dislocation density. The climbing segments of the dislocations finally reach the corner of the  $\gamma'$  cube, where they are released into the channel crossing where they eventually annihilate. This results in a drop of the dislocation density at the transition from regime (B) to regime (C).

After the escape of the dislocation from the narrow channel, the dislocation density further increases. It then levels off at the end of regime (C), because the next  $\gamma'$  cube then impedes the motion of the dislocation. The magnitude of the applied stress is 150 MPa which results in a maximum resolved shear stress (MRSS) of  $\sim 61$  MPa on the dislocation glide plane. This value is too low to overcome the stress of  $\tau_{or} \approx \mu b/w = 116$  MPa that would be required for the dislocation to be squeezed into the next  $\gamma$  channels of width  $w = 80$  nm.

### 3.2. Climb rate effect

The DDD simulation of creep in a single-crystal Ni base superalloy is conducted using a homogeneous starting distribution of the  $1/2a_0\langle 011 \rangle\{1\bar{1}1\}$  mixed dislocations over 12 slip systems with an average dislocation density of  $\sim 6.7 \times 10^{13} \text{ m}^{-2}$  in the simulation box. A constant tensile stress of 150 MPa is applied along the  $[100]$  crystallographic direction. Three different glide/climb mobility ratios representing three different temperatures are used. Plastic strain as a function of simulation time is plotted in Fig. 4a for three different climb mobilities. The graph reveals a rapid increase in the strain magnitude at the

beginning of creep, independent of the choice of the glide/climb mobility ratio. This relates to the unconstrained movement of dislocations in the  $\gamma$  channels before they reach the  $\gamma/\gamma'$  interface (regime A).

After this first stage, the influence of the climb rate becomes apparent in terms of different plastic creep strains for the different  $M_g/M_c$  ratios. For the lowest climb mobility, i.e.,  $M_g/M_c = 1000$ , the plastic strain levels off when the dislocations reach the  $\gamma'$  cube. Similarly also for the mobility ratio of  $M_g/M_c = 100$ , the creep strain levels off, but at a relatively large plastic strain of  $\sim 0.05\%$ . Later, for both cases, the creep strain increases slightly with time. When the climb mobility increases by one or more orders of magnitude to a value of  $M_g/M_c = 10$ , the creep strain steadily increases as a function of simulation time (Fig. 4a). The average strain rates for the three glide/climb mobility ratios are 0.06, 0.09 and  $0.92 \text{ s}^{-1}$  with increasing climb mobility, respectively. This shows that an exponential increase in the climb mobility results in a corresponding exponential increase in the strain rate, although with a different factor.

The variation in the dislocation density as a function of simulation time for different glide/climb mobility ratios at an applied stress of 150 MPa is shown in Fig. 4b. The beginning of creep is always associated with a recovery step, caused by a reduction in dislocation density. For higher dislocation climb rates, the drop in dislocation density is faster. For the two lower climb rates, i.e., for  $M_g/M_c = 100$  and 1000, the dislocation density decreases to a minimum, where it remains relatively constant with only minor variations.

This transition into an apparently steady-state regime with low dislocation density can be explained as follows. The increase in the climb rate obviously assists the recovery of dislocations at 150 MPa, but this stress is not high

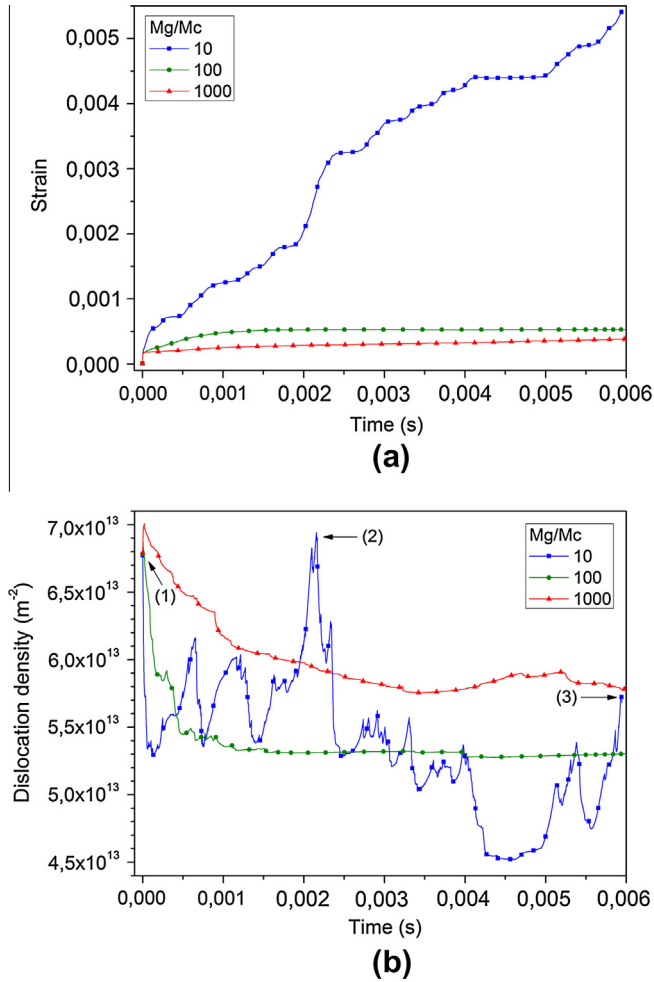


Fig. 4. (a) Equivalent strain and (b) dislocation density as a function of simulation time for the creep DDD simulation of 59%  $\gamma'$  volume fraction at an applied stress of 150 MPa, using different glide/climb mobility ratios. Arrows in image (b) indicate those simulation times for which corresponding microstructures are shown in Fig. 9.

enough to force the dislocations into the  $\gamma$  channels. As mentioned above, the critical stress for squeezing a dislocation into a channel amounts, for the present model system, to  $\sim 116$  MPa, whereas the applied MRSS reaches a value of only 61 MPa. Despite the observed behavior for the cases with the two lowest climb rates, Fig. 4b reveals that, when the climb rate increases further to a ratio of  $M_g/M_c = 10$ , fluctuations in the dislocation density appear. Although dislocations are annihilated faster than in the other two cases, the highest climb rate assists in climb of dislocations through the  $\gamma$  channels along the  $\gamma/\gamma'$  interfaces. The evolution of this part of the dislocation substructure is observed for those dislocations that are aligned along those  $\gamma/\gamma'$  interfaces perpendicular to the  $[100]$  loading direction.

Using a glide/climb mobility ratio of  $M_g/M_c = 10$ , the dislocation density at  $\sim 0.2\%$  creep strain is comparable with the dislocation density at the beginning of the simulation, as shown by the arrows (1) and (2) in Fig. 4b. A pre-

vious study by Vattré et al. [80,81] suggested that, under strain rate controlled deformation of a Ni base superalloy along the  $[001]$  direction, the dislocation density increases with increasing strain. Starting with a dislocation density comparable with the one used in the present microstructure, i.e.,  $6.7 \times 10^{13} \text{ m}^{-2}$ , they showed that, after 0.2% plastic strain, the dislocation density exceeds the initial one by a factor of 4. This plastic strain is achieved at higher MRSS levels than the critical stress required for entering the  $\gamma$ -channel. Therefore, It is concluded that, when applying a climb mobility that amounts to 10% of the glide mobility, the material deforms at an applied stress much below the critical stress, so that the tendency to form a regular dislocation network is not very pronounced. This is in agreement with experimental results on creep of typical Ni base superalloys at  $\sim 1000$  °C [9–32]. The dislocation mechanisms observed in the current DDD simulations associated with this deformation stage are analyzed below in more detail.

### 3.3. Effect of the applied stress

As discussed in the preceding section, the low applied stress makes it difficult for dislocations to squeeze into the  $\gamma$  channels and, therefore, also hampers the formation of a dislocation network. Here, the effects of the applied stress are investigated for a glide-to-climb mobility ratio of  $M_g/M_c = 10$  on the creep deformation of Ni base superalloys. The strain response at stresses of 150, 250 and 350 MPa, respectively, as a function of simulation time is shown in Fig. 5a. For all stress levels, the plastic strain increases monotonically. At a given time, for a higher applied stress, higher plastic strain accumulates. The predicted increase in plastic strain is lowest for the smallest stress level (150 MPa).

The resultant MRSS for the applied  $[100]$  tensile stresses are 61, 102 and 143 MPa, respectively. For the two smaller tensile stresses imposed, these values are below the critical stress required for squeezing dislocations into the  $\gamma$  channels (116 MPa). Only for the largest applied tensile stress should squeezing of dislocations into the channels be possible.

Fig. 5b shows the evolution of dislocation densities with time for the three applied stress levels. Dislocation recovery rates similar to those observed for 150 MPa in Fig. 5 can be seen for 250 MPa at the onset of creep. For the two lowest applied stress levels with a resolved stress below the critical squeezing stress, dislocation recovery is the dominant mechanism that governs microstructure evolution. In the case of 250 MPa applied stress, the dislocation density increases slightly after passing through an initial minimum. It eventually adopts a relatively stable value of  $\sim 8 \times 10^{13} \text{ m}^{-2}$ . In contrast, at an applied stress of 350 MPa, the dislocation density increases from the beginning on. At first, it increases very rapidly by nearly a factor of 2, and then it increases further with a slower yet relatively constant slope. This means that, when the applied

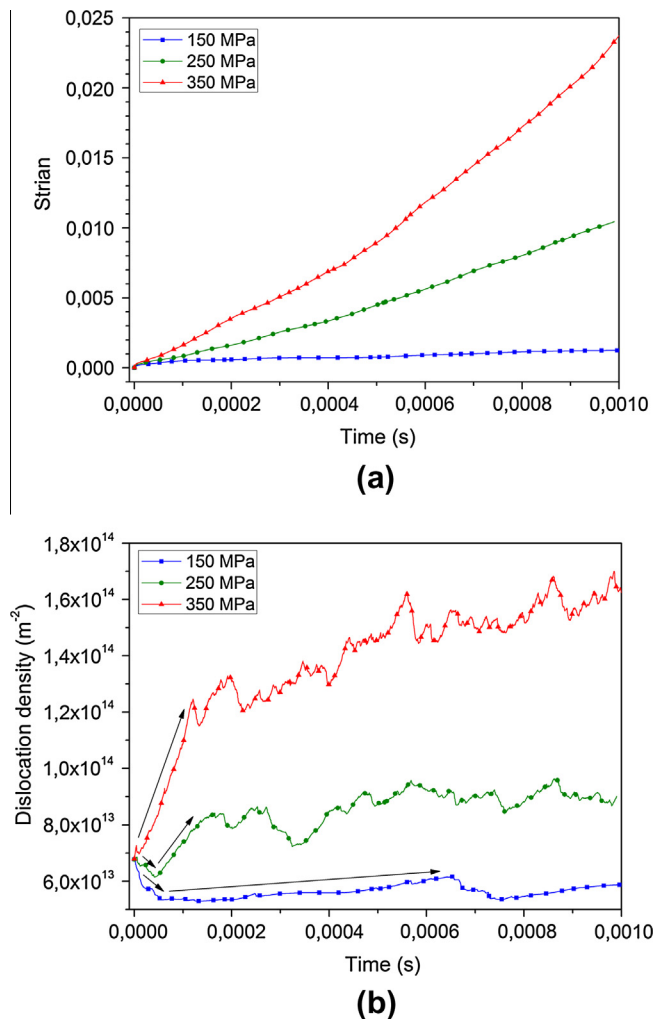


Fig. 5. (a) Equivalent strain and (b) dislocation density as a function of simulation time for a creep DDD simulation for a sample with 59%  $\gamma'$  volume fraction at different applied uniaxial stresses using a glide/climb mobility ratio of  $M_g/M_c = 10$ .

stress is above the critical stress, the dislocation density keeps increasing. In contrast, for the two low-load cases, where stresses are not sufficiently high to promote channel dislocation glide, the dislocation density fluctuates without a notable increase over time after the initial recovery regime.

This analysis of the evolution of the dislocation density is essential for understanding the transition in the creep mechanism, which cannot be rationalized merely on the basis of the results presented in Fig. 5a. It is concluded that the plastic creep deformation that is observed at applied stresses below the critical stress for dislocations required for entering the  $\gamma$ -channel (determined by the channel width) critically depends on the climb mobility in the high-temperature creep regime of Ni base superalloys. At higher applied stresses, in contrast, the glide controlled motion of dislocations that squeeze into the channels contributes significantly.

The variation in strain rate as a function of simulation time is shown in Fig. 6 for different applied stresses. These diagrams reveal that, at the early stages of deformation, the strain rate drops by about one order of magnitude. For the two low-load cases, the strain rate reaches a minimum and then remains relatively constant. This minimum depends on the level of the applied stress and the glide/climb mobility ratio. A similar behavior is also observed at the lowest applied stress, i.e., 150 MPa, with different glide/climb mobility ratios. For the high load case, however, the strain rate increases gradually as a function of time. This difference between the low- and high-stress regimes relates to the contribution of dislocation multiplication to the strain rate variations in the high-stress regime, as shown in Fig. 5b. When the dislocation density increases, the newly generated dislocations could further promote a higher creep rate. Therefore, as a result, any process limiting dislocation multiplication would limit the creep rate as well. This is particularly important, since an increase of two orders of magnitude in climb rate, from  $M_g/M_c = 1000$  to  $M_g/M_c = 10$ , where no large change in the dislocation density is observed, leads to stable strain rate variations about the average value reported in the preceding section. When loading with an applied stress level that enables locally reaching the critical stress required for squeezing dislocations into the  $\gamma$  channels, the dislocation density increases, resulting in a strain rate rise as a function of time.

Owing to the relatively high strain rates of the current DDD simulations, a direct comparison with experimental findings is not straightforward. However, a qualitative comparison suggests that the trend of the predicted variation in the strain rate as observed in Fig. 6 is similar to experimental observations [9,22–32]. These previous experimental studies of Ni base superalloys similarly show that an early rapid drop is eventually followed by a slight increase in the strain rate with increasing time.

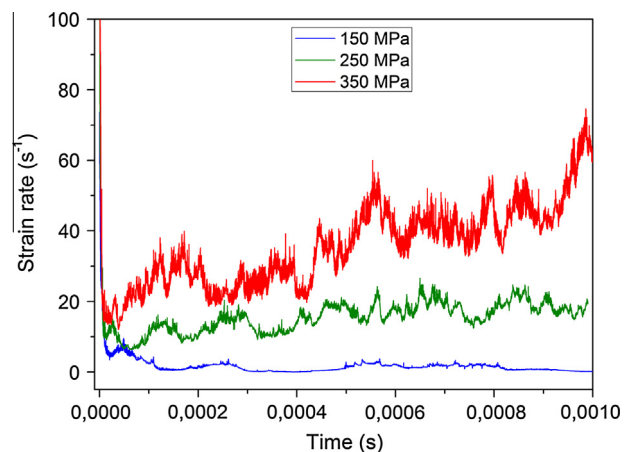


Fig. 6. Strain rate as a function of simulation time for the DDD simulation of a sample with 59%  $\gamma'$  volume fraction at different applied uniaxial stresses using a glide/climb mobility ratio of  $M_g/M_c = 10$ .



### 3.4. Effect of simulation conditions

#### 3.4.1. Initial conditions

Here, the influence of the initial conditions on the predictions is investigated. First, consider the effects of the initial dislocations microstructure (IDM) on the calculated creep strain and dislocation density. Second, the effect of the simulation cell size containing eight  $\gamma'$  particles in comparison with results obtained from using a simulation cell with only one  $\gamma'$  particle is discussed.

To identify IDM effects on the results, two different random initial dislocation arrangements are created in addition to the one that led to the results shown in Figs. 4–6, but using the same initial dislocation density in all cases. The results of equivalent creep plastic strain and dislocation density are given in Fig. 7. It appears that, for the glide/climb mobility ratio of  $M_g/M_c = 10$ , the microstructure evolution predicted for applied stresses of 150 and

350 MPa, respectively, along the [100] direction is comparable. At the applied stress of 350 MPa, the monotonic increase in the creep strain and the variations in dislocation density are similar for all three IDM. At 150 MPa, a similar low creep strain and an initial drop with later fluctuations in the dislocation density are also seen. Using different IDM, therefore, leads only to small quantitative differences and fluctuations in the creep strain and dislocation density values. It should be noted that employing one unique IDM throughout this study prevents any artificial effects of the IDM on the final conclusions of the DDD simulations.

#### 3.4.2. Boundary conditions and simulation box size

Dislocations are transferred from one side of the simulation box to the opposite side through the PBC employed in the current DDD simulations. Although the dislocation climb prohibits self-annihilation due to PBC, other effects such as dislocation self-interaction may occur as a result of the boundary conditions applied along the narrow  $\gamma$  channels. Therefore, an additional effort was made to simulate creep using a larger simulation box of 1000 nm side length. As a starting condition, a dislocation density similar to that used in the previous simulations was distributed over all 12 channel slip systems of the simulation box with eight  $\gamma'$  particles of size 420 nm. All other simulation conditions were kept constant. The load is 350 MPa applied along the [100] direction with a glide-to-climb ratio of  $M_g/M_c = 10$ . The evolution of plastic strain and dislocation density for this calculation is shown in Fig. 8. The results reveal that the large sample yields a slightly lower plastic deformation and dislocation density at a given simulation time than predicted for the one-particle model. It is also observed that the simulation for the sample containing eight particles predicts a more monotonic increase in strain and dislocation density compared with the simulations with only one  $\gamma'$  cube.

These simulation box size effects observed in Fig. 8 can be attributed mainly to two reasons: First, using a simulation cell with eight  $\gamma'$  particles averages and smooths over the various microstructure mechanisms and thus leads to slightly different dislocation configurations around each particle. Second, the use of PBC can potentially cause different dislocation self-interaction effects compared with the case where a single-particle cell is used. If the simulation sample contains only one  $\gamma'$  particle, the dislocation self-interaction effects are mostly confined to regions near the simulation cell boundaries. This effect leads to larger fluctuations in the plastic strain and dislocations density compared with the eight particles simulation box. The two different supercell setups may thus experience different types of dislocations self-interaction effects through the use of PBC.

Irrespective of these slight differences pertaining to the simulation box size, it should be noted that the slightly higher plastic strain and dislocation density observed for the single-particle simulation case falls mainly inside the scatter that is associated with the use of different random IDM. This influence is shown in Fig. 7.

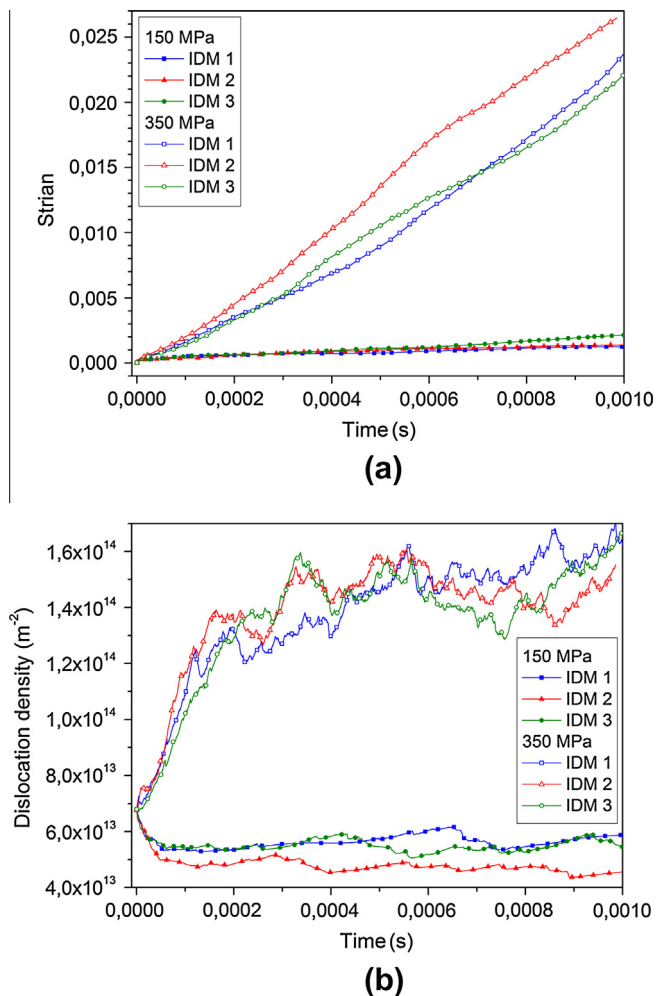


Fig. 7. Predicted (a) plastic strain and (b) dislocation density as a function of simulation time in DDD simulated creep tests for two different applied stresses, namely, 150 and 350 MPa, and a glide/climb mobility ratio of  $M_g/M_c = 10$  using three different random IDM. The latter variation in the initial conditions was conducted in order to study the influence of statistical effects associated with the starting dislocation microstructure on the predicted creep rates.

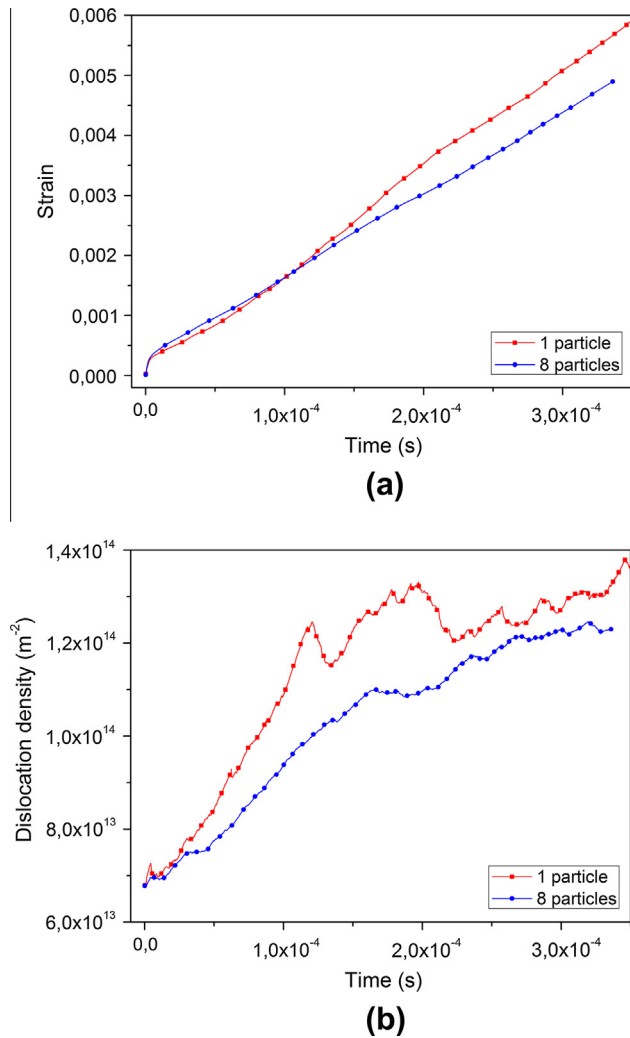


Fig. 8. Predicted (a) plastic strain and (b) dislocation density as a function of simulation time in a DDD simulated creep test at 350 MPa applied stress and a glide/climb mobility ratio of  $M_g/M_c = 10$ , using different simulation box sizes of length 500 nm and 1000 nm, including one and eight  $\gamma'$  cubes, respectively.

Finally, it should be mentioned that this study used an approximate ratio of the glide-to-climb mobility to mimic temperature effects in Ni base superalloy creep. In order to obtain a more quantitative prediction of the creep deformation in direct comparison with experiments, a dislocation climb mobility law may be implemented into the DDD simulation code to fully account for the dislocation climb through vacancy diffusion and its coupling with the dislocation glide [68,86].

#### 4. Microstructure analysis

##### 4.1. Low-stress creep regime

Fig. 9 shows the microstructure evolution at 150 MPa and a glide-to-climb mobility ratio of  $M_g/M_c = 10$ . The simulated microstructures at the three different stages indicated by arrows in Fig. 4b are shown, namely: the onset of deformation representing the initial dislocation microstructure; an intermediate stage where the dislocation density rises to a local maximum; and the final creep microstructure. Arrows in Fig. 9b indicate the nano-sized dislocation loops that form on the edges and corners of the  $\gamma'$  cube. These snapshots demonstrate a typical creep microstructure after low-stress and high-temperature creep with an initial dislocation density of  $6.7 \times 10^{13} \text{ m}^{-2}$ . Despite the initial rapid dislocation recovery, shown in Fig. 4b, the dislocation substructure develops by climb of dislocations along the  $\gamma$  channel. Owing to the low applied stress, the dislocations do not enter the  $\gamma$  channels when their line direction crosses the  $\gamma'$  cube. This leads to a creep microstructure with long bent dislocations that are formed along the edges and faces of the  $\gamma'$  cube. Dislocation reactions mainly occur at the regions near the corners of the  $\gamma'$  cube. The dislocations are able to react with each other and form different types of junctions that can later be eliminated by recombination with other incoming dislocations or by unzipping processes. Such a forest of dislocations can be

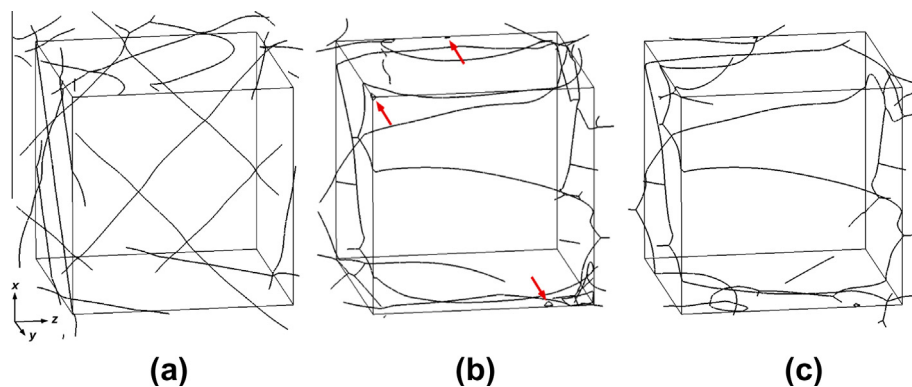


Fig. 9. Simulated microstructure of the single-crystal Ni base superalloy at 150 MPa in  $x = [100]$  direction, using a glide/climb mobility ratio of  $M_g/M_c = 10$  at three different simulation times shown by the arrows in Fig. 4. (a) Onset of deformation representing the initial microstructure of straight dislocations lying along  $\langle 110 \rangle$  directions; (b) intermediate stage where the dislocation density rises up to a maximum; and (c) final microstructure deformed to 0.5% creep strain. The arrows in image (b) show the small dislocation loops that are formed on the edge and corner of the  $\gamma'$  cube.

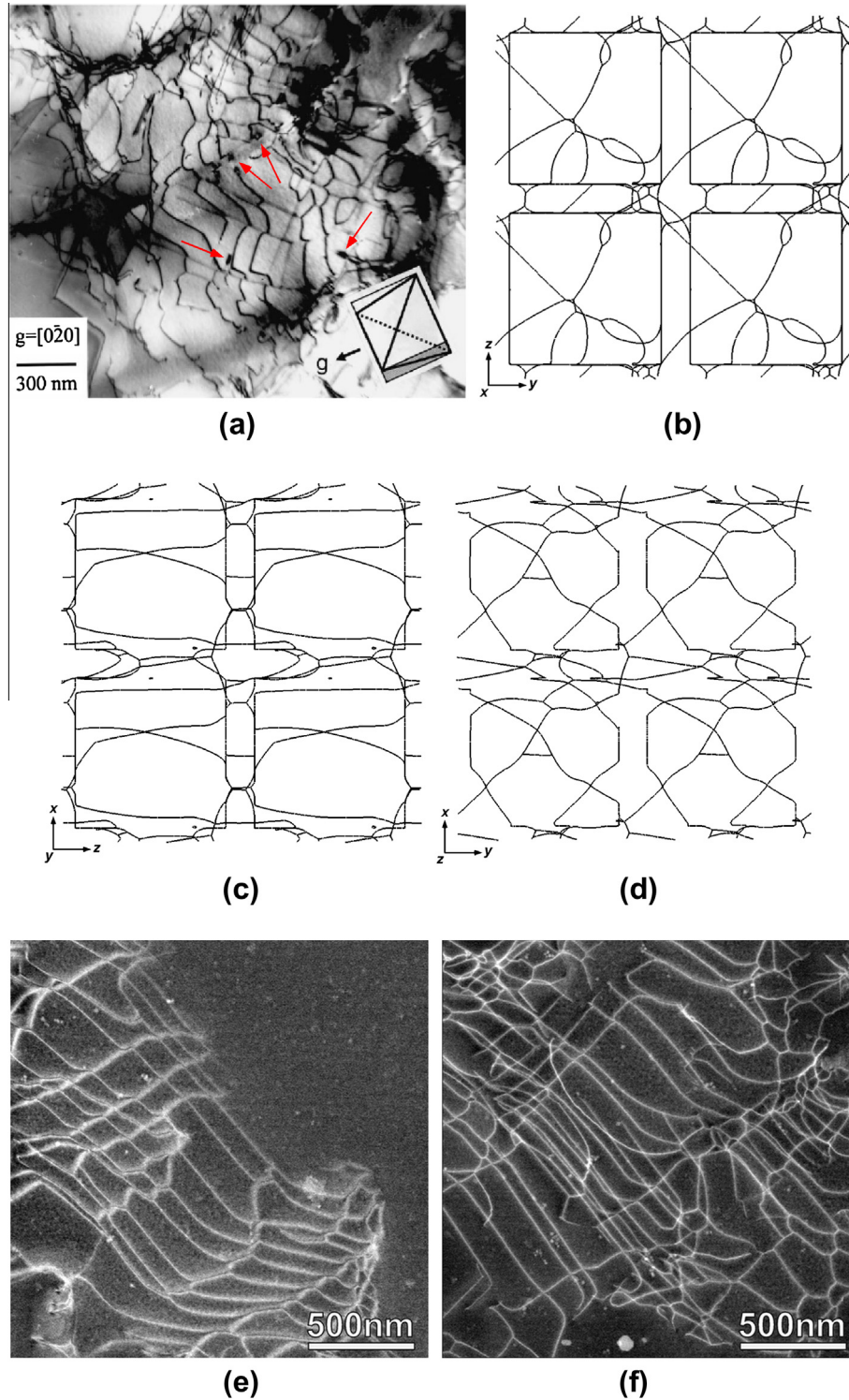


Fig. 10. (a) Experimental microstructure of a Ni base superalloy in primary creep stage at 85 MPa shear loading condition taken from Ref. [31]. The objects indicated by the arrows show the small dislocation loops that formed during creep. (b–d) Predicted creep microstructure of a single-crystal Ni base superalloy deformed to a creep strain of 0.5% at 150 MPa, low-stress regime, loading along  $x=[100]$  direction observing the entire simulated microstructure through (b)  $x$ , (c)  $y$  and (d)  $z$  directions. The simulated sample is replicated in three dimensions for better visualization of the dislocations in the  $\gamma$  channels. A glide/climb mobility ratio of  $M_g/M_c = 10$  is assumed for these simulations. (e, f) Similar microstructures observed by multibeam DF-STEM diffraction contrast characterization of a single-crystal Ni base superalloy sample exposed to 160 MPa, along  $[110]$ , deformed to a total creep strain of 0.1% [87].

seen in Fig. 9b in the two right-hand corners of the  $\gamma$  particle.

Experimental work of Kolbe et al. [31] shows a microstructure in the low-stress and high-temperature regime



during primary creep of a CMSX6 superalloy that is comparable with the current simulation results. An example of this microstructure is shown in Fig. 10a. The material was deformed with 85 MPa shear loading along a plane parallel to the image surface at a temperature of 1025 °C. The objects highlighted by the arrows in this image relate to the nanoscopic polygonal loops formed during creep. These polygonal dislocation loops are comparable with those shown in Fig. 9b. Here, the focus is first on the final creep microstructure shown in Fig. 9c, observing the entire simulated microstructure through three different directions, namely  $x$ ,  $y$  and  $z$ , as shown in Fig. 10b–d. The simulated microstructure is replicated in three dimensions for better visualization of the dislocation network in the  $\gamma$  channels. These images reveal fair similarity to the experimental creep microstructure shown in Fig. 10a, although the loading condition is different. The experimental and simulated microstructures both show long, bent dislocations, particularly in the  $\gamma$  channels between the  $\gamma'$  cube faces. This feature of the dislocations relates to the climb process that moves them out of their initial glide planes. The DDD results show that the bent dislocations are indeed observed mainly in the  $\gamma$  channels perpendicular to the loading direction, i.e., along the  $x = [100]$  direction in Fig. 10b. The apparent net cubic-type slip that is due to the coupled glide–climb dislocation motion used in this simulation contributes to the curved shape of the dislocations in those channels, whereas the dislocations in the  $\gamma$  channels along the loading direction are deposited mainly along  $\gamma/\gamma'$  interfaces (e.g., see Fig. 10c and d). PK force calculations reveal that, in the latter case, owing to the alignment of the dislocation line direction and Burgers vector direction relative to the applied stress, the climb force pushes the dislocation

towards the  $\gamma/\gamma'$  interface rather than in opposite direction. Therefore, the climb force does not contribute to the sliding of dislocations along the  $\gamma/\gamma'$  interface. This is similar to the interaction of a single dislocation with the  $\gamma'$  particle observed in Fig. 1, where the two side arms of the gliding dislocation are bowed out into the  $\gamma$  channels and deposit along the interfaces parallel to the loading direction that is along  $y$ . These dislocations are locked mainly at the hetero-interfaces, and they may interact and recombine with the dislocations entering from the horizontal channel, particularly near the corners and edges of the  $\gamma'$  particle. Fig. 10e and f shows similar microstructures observed by TEM [87: new quote] conducted on a single-crystal Ni base superalloy sample exposed to 160 MPa and deformed to a total creep strain of 0.1% along [110].

#### 4.2. High-stress creep regime

Fig. 11a shows 3D and two-dimensional (2D) views of the predicted creep microstructure of the Ni base superalloy deformed to 0.5% strain at 350 MPa along the  $x$  direction, using a climb/glide mobility ratio of  $M_g/M_c = 10$  in the 1000 nm simulation sample. The microstructure shows deposited dislocations at the  $\gamma/\gamma'$  interfaces perpendicular to  $y$  and  $z$ , whereas the dislocations in the  $\gamma$  channels perpendicular to the loading direction have mainly curved shapes, without being clearly deposited at the  $\gamma/\gamma'$  interface, as can be seen from the 3D image of Fig. 11a. Investigation of the DDD results reveals that the dislocations located in these channels are mobile and that they move by a coupled glide–climb mechanism when they approach the  $\gamma/\gamma'$  interfaces. However, in the channels along the tensile direction for the case of 350 MPa applied stress, i.e.,

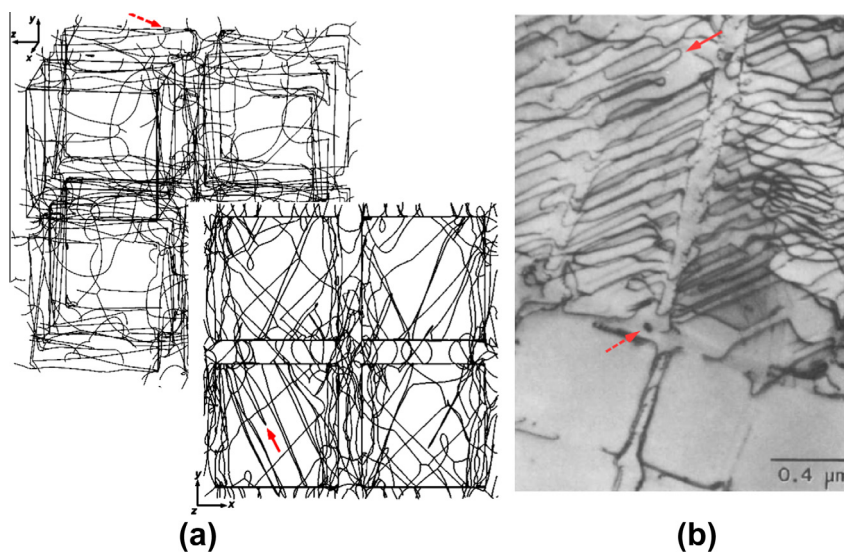


Fig. 11. (a) 3D and 2D view of the DDD simulated creep microstructure of a Ni base single-crystal superalloy exposed to a loading condition of 350 MPa, high-stress regime, along the  $x = [100]$  direction using a climb/glide mobility ratio of  $M_g/M_c = 10$ . (b) Experimental creep microstructure of Ni base superalloy at loading conditions of 552 MPa along  $[001]$  direction taken from Ref. [13]. In both the DDD simulations and the experimentally observed microstructures, the solid tail arrow indicates an example of a dislocation squeezing into the  $\gamma$  channel and the dashed tail arrow indicates a polygonal dislocation loop.



above the critical squeezing stress, dislocations are able to penetrate the  $\gamma$  channels and deposit segments along the  $\gamma/\gamma'$  interfaces. Similar dislocation mechanisms have been observed experimentally, e.g., by Pollock and Argon [13]. They studied a CMSX3 Ni base superalloy in the high-stress creep regime exposed to 552 MPa along the  $[001]$  direction, as shown in Fig. 11b. In both the DDD and the experimental study, the microstructures consist of dislocations deposited at the  $\gamma/\gamma'$  interfaces with line orientations near the  $\langle 110 \rangle$  directions. An example of dislocation penetration into the  $\gamma$  channel is indicated by a solid arrow for both the DDD simulation and the experimental microstructures. In addition, similar to the low-stress creep microstructure depicted in Fig. 10, polygonal dislocation loops are observed in both the DDD simulation and in the real microstructure after high-stress creep. One of those dislocation loops is highlighted by a dashed arrow in both microstructures.

#### 4.3. Polygonal dislocation loop formation

The occurrence of polygonal dislocations loops in both the low- and high-stress DDD creep simulations was highlighted in the previous sections. This feature is comparable with the experimentally observed dislocation loops reported in previous Ni base superalloy creep studies [22–33]. Here, one of those loops in the top-left-front corner of the  $\gamma'$  cube in Fig. 9b is closely examined.

The sequence of the triangular dislocation loop formation in the corner of the  $\gamma'$  cube is illustrated in Fig. 12. Snapshots of Fig. 12a–e show how a mixed dislocation with  $b = 1/2a_0[101]$  glides in the  $(100)$   $\gamma$  channel towards a  $\gamma'$  cube. Its two arms spread into the lateral  $\gamma$  channels when it reaches to the  $\gamma'$  particle. By forcing the two arms

into the neighboring  $\gamma$  channels, they deposit dislocation segments along the  $(010)$  and  $(001)$  surfaces of the  $\gamma'$  cube when moving further. Finally, at step (e), the two dislocation segments of different sign approach each other and annihilate. By annihilation of the two opposite sign segments, the dislocation is released, leaving behind a triangular dislocation wrapping around the corner of the  $\gamma'$  cube.

After the formation of the dislocation loop, it may interact with other moving dislocations. As it appears in the early stage snapshots of the triangular dislocation, there is a second dislocation that is gliding in the same glide plane as the first one, approaching from the top-right corner of the images. This dislocation reaches the previously formed dislocation loop at the cube corner and experiences a repulsive force (Fig. 12f). The present investigation shows that this second dislocation has the same Burgers vector as the corner dislocation, but with an opposite sign. Later on in Fig. 11g–i, by further glide of the entire dislocation line, it repels the locked segments of the dislocation loop along the  $(001)$  and  $(100)$  interfaces of the  $\gamma'$  cube. This leads to its shrinkage to a size as small as seen in Fig. 12j. No further shrinkage and annihilation of the dislocation loop is observed, since the second dislocation reacts with a third dislocation that can be seen in the right side of image (j). It changes the direction of the dislocation's motion and avoids further annihilation of the dislocation loop. Therefore, the triangular dislocation loop remains in the final shape that is seen in Fig. 12j. This small dislocation loop is stable, since for the segment depositing along the  $(001)$   $\gamma/\gamma'$  interface, neither the glide–climb force nor the climb force alone is directed towards the  $\gamma$  channel to mobilize it along the interface. This is similar to the force conditions seen in Fig. 1, when the mixed dislocation reaches the interface parallel to the applied stress at position B. None of the

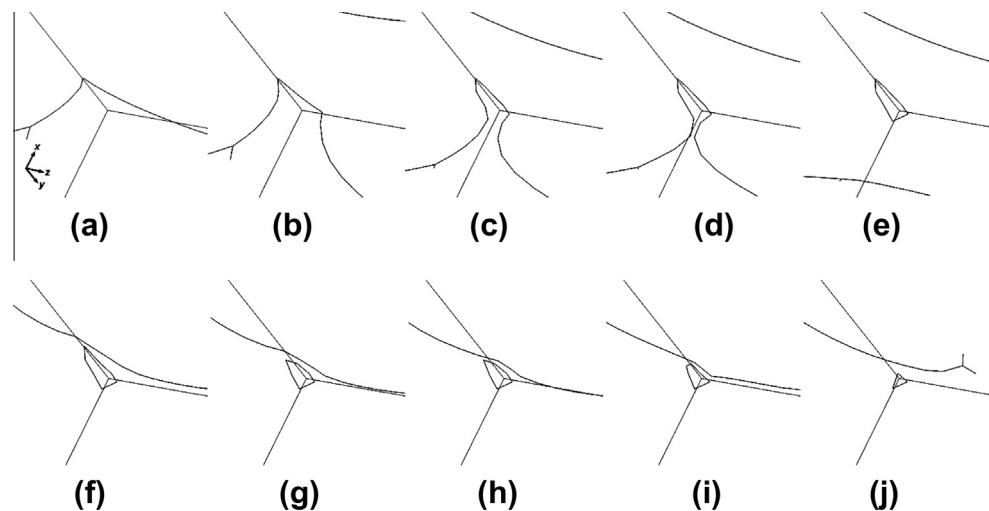


Fig. 12. Mechanism of dislocation loop formation on the top-left-front corner of the  $\gamma'$  cube shown in Fig. 9b: (a–d) glide of a mixed dislocation with  $b = 1/2a_0[101]$  on the  $(100)$  interface and two lateral arms bending into the neighboring  $\gamma$  channels, where they deposit on the  $(010)$  and  $(001)$  interfaces; (e) dislocation release from the corner of the  $\gamma'$  cube; (f–i) the interaction of a second dislocation gliding with a similar sense of the previous dislocation but with opposite Burgers vector,  $b = -1/2a_0[101]$ . It repels the locked segment of the dislocation loop on the  $(100)$  interface, causing its shrinkage to the smallest size seen in (j).

two forces shown in this illustration moves the dislocation away from the interface at position B. Therefore, such types of segments would lock the small polygonal loop prohibiting their annihilation at the corner, despite the strong line tension that is created by the neighboring segments. Other dislocation loops are also formed as a result of similar interactions with the edges and corners of the  $\gamma'$  cube and with other dislocations.

## 5. Concluding remarks and outlook

DDD simulations were used to study the relative importance of glide and climb processes in the early stages of high-temperature and low-stress creep of single-crystal Ni-based super alloys where dislocation plasticity is confined to the thin  $\gamma$  channels. A model system and loading regime were studied, where elastic misfit and  $\gamma'$  cube cutting processes were neglected. As a consequence, strain hardening was associated mainly with dislocation density increase and recovery mechanisms of dislocations at  $\gamma'$  particle corners. From the modeling results, the following main conclusions can be drawn.

1. The DDD model correctly mimics the interaction of an octahedral  $\gamma$  channel dislocation with a cuboidal  $\gamma'$  precipitate. It shows that the movement of dislocations along the  $\gamma/\gamma'$  interface close to the  $\gamma'$  cube can be interpreted as a combination of dislocation glide and climb. It does not seem appropriate to address this movement as cube slip; while an observer could have the impression that the dislocation glides on a  $\{100\}$  plane, the underlying physical nature is a microscopic coupling of glide and climb. This means that this type of net dislocation motion is climb controlled and slow. The dislocation is released when reaching the  $\gamma'$  corner.
2. Promoting climb vs. glide in the DDD model, where initially a total  $\gamma$  channel dislocation density of  $6.7 \times 10^{13} \text{ m}^{-2}$  is evenly distributed over 12 microscopic crystallographic slip systems, results in higher accumulated creep strains. This applies to microscopically resolved shear stress loads that are lower than the critical stress required for squeezing a dislocation into the channel. When the climb mobility is reduced, creep strain accumulation decreases. This result is in line with the view that dislocation climb determines the overall creep rate.
3. A critical stress is observed, below which recovery processes result in a decrease in the total dislocation density. Above this critical stress dislocation, multiplication occurs. Both processes affect the creep rate. The creep mechanism below the critical stress is controlled mainly by the climb process, whereas for loads above the critical stress, dislocation multiplication associated with the squeezing of dislocation loops into thin  $\gamma$  channels is the controlling creep mechanism.
4. The influence of the boundary conditions on the DDD predictions was studied. Comparing two different cases, viz. 500 nm box size including one  $\gamma'$  particle and 1000 nm box size including eight  $\gamma'$  particles, it is found that the larger simulation volume yields results that are in better agreement with experiments.
5. Microstructure analysis of the simulated low-stress creep results reveals that the creep microstructure of a single-crystal Ni base superalloy consists mainly of long bent dislocations in the inter-particle spacing. This is in agreement with previous experimental observations. Complex dislocation tangles may form near the corners of  $\gamma'$  cubes, where dislocations from vertical and horizontal channels can react.
6. The microstructure of the high-stress creep simulations also shows good qualitative agreement with previous experimental observations. The simulated microstructure consists of deposited dislocations along near- $\langle 110 \rangle$  directions on the  $\gamma/\gamma'$  interfaces that are parallel to the loading conditions and mobile dislocations in the channels and at the interfaces perpendicular to the loading direction.

In the future, the present authors suggest incorporating in future simulations more of the complexities that characterize real microstructures in these materials, such as the effects of misfit stresses and different  $\gamma'$  particle dispersions. The simplifications made in the current model were required to conduct a first approach of including elementary dislocation mechanisms that govern creep of Ni base single-crystal superalloys considering the characteristic features of the 3D microstructure and dislocation climb.

## Acknowledgements

The authors are grateful for funding by the Deutsche Forschungsgemeinschaft DFG through Projects A1, A2 (G.E.) and A4 (D.R.) of the collaborative research center SFB/TRR 102 on single-crystal super alloys. We acknowledge L. Agudo Jácome for supporting our DDD simulations with the TEM characterizations and his helpful comments on this work. S.M.H.H. acknowledges funding by the Max-Planck Society through the Max-Planck Fellow group High Temperature Materials at the Max-Planck Institut für Eisenforschung in Düsseldorf.

## References

- [1] Ilshner B. Hochttemperatur-Plastizität Warmfestigkeit und Warmverformbarkeit metallischer und nichtmetallischer Werkstoffe. Berlin: Springer; 1973.
- [2] Cadek J. Creep in metallic materials. Amsterdam: Elsevier; 1988.
- [3] Nabarro FRN, De Villiers HL. The physics of creep: creep and creep-resistant alloys. London: Taylor & Francis; 1995.
- [4] Reed RC. The superalloys: fundamentals and applications. Cambridge: Cambridge University Press; 2008.
- [5] Reed RC, Matan N, Cox DC, Rist MA, Rae CMF. Acta Mater 1999;47:3367.

- [6] Heilmaier M, Krüger M, Saage H, Rösler J, Mukherji D, Glatzel U, et al. JOM 2009;61:61.
- [7] Reed RC, Yeh AC, Tin S, Babu SS, Miller MK. Scripta Mater 2004;51:327.
- [8] Reed RC, Cox DC, Rae CMF. Mater Sci Eng A 2007;448:88.
- [9] Mayr C, Eggeler G, Dlouhy A. Mater Sci Eng A 1996;207:51.
- [10] Malzer G, Hayes RW, Mack T, Eggeler G. Metall Mater Trans A 2007;38:314.
- [11] Raujol S, Benyoucef M, Locq D, Caron P, Pettinari F, Clement N, et al. Philos Mag 2006;86:1189.
- [12] Carry C, Strudel JL. Acta Metall 1977;25:767.
- [13] Pollock TM, Argon AS. Acta Metall Mater 1992;40:1.
- [14] Lahrman DF, Field RD, Darolia R, Fraser HL. Acta Metall 1988;36:1309.
- [15] Feller-Kniepmeier M, Link T. Metall Trans A 1989;20:1233.
- [16] Keller RR, Maier HJ, Mughrabi H. Scripta Metall Mater 1993;28:23.
- [17] Völkl R, Glatzel U, Feller-Kniepmeier M. Acta Mater 1998;46:4395.
- [18] Saß V, Glatzel U, Feller-Kniepmeier M. Acta Mater 1996;44:1967.
- [19] Müller L, Glatzel U, Feller-Kniepmeier M. Acta Metall Mater 1993;41:3401.
- [20] Müller L, Glatzel U, Feller-Kniepmeier M. Acta Metall Mater 1992;40:1321.
- [21] Gleiter H, Hornbogen E. Acta Metall 1965;13:576.
- [22] Eggeler G, Dlouhy A. Dlouhy, Acta Mater 1997;45:4251.
- [23] Link T, Epishin A, Bruckner U. Scripta Mater 1998;39:1463.
- [24] Link T, Epishin A, Klaus M, Bruckner U, Reznicek A. Mater Sci Eng A 2005;405:254.
- [25] Epishin A, Link T. Philos Mag 2004;84:1979.
- [26] Kostka A, Malzer G, Eggeler G. J Microsc 2006;223:295.
- [27] Kostka A, Malzer G, Eggeler G, Dlouhy A, Reese S, Mack T. J Mater Sci 2007;42:3951.
- [28] Sarosi PM, Srinivasan R, Eggeler G, Nathal MV, Mills MJ. Acta Mater 2007;55:2509.
- [29] Pollock TM, Argon AS. Acta Metall Mater 1994;42:1859.
- [30] Nabarro FRN. Metall Mater Trans A 1996;27:513.
- [31] Kolbe M, Dlouhy A, Eggeler G. Mater Sci Eng A 1998;246:133.
- [32] Probst-Hein M, Dlouhy A, Eggeler G. Acta Mater 1999;47:2497.
- [33] Srinivasan R, Eggeler G, Mills MJ. Acta Mater 2000;48:4867.
- [34] Glatzel U, Feller-Kniepmeier M. Scripta Metall 1989;23:1839.
- [35] Rae CMF, Reed RC. Acta Mater 2007;55:1067.
- [36] Lefebvre S, Devincre B, Hoc T. J Mech Phys Sol 2007;55:788.
- [37] Ahmed N, Hartmaier A. Acta Mater 2011;59:4323.
- [38] Zhu Z, Basoalto H, Warnken H, Reed RC. Acta Mater 2012;60:4888.
- [39] Yashiro K, Naito M, Tomita Y. Int J Mech Sci 2002;44:1845.
- [40] Tinga T, Brekelmans WAM, Geers MGD. Model Simul Mater Sci 2010;18:051005.
- [41] Staroselsky A, Cassenti BN. Mech Mater 2010;42:945.
- [42] Fedelich B. Int J Plast 2002;18:1.
- [43] Djuansjah JRP, Yashiro K, Tomita Y. Mater Trans 2008;49:2507.
- [44] Zambaldi C, Roters F, Raabe D, Glatzel U. Mater Sci Eng A 2007;454–455:433.
- [45] Ma A, Roters F, Raabe D. Acta Mater 2006;54:2169.
- [46] Ma A, Roters F, Raabe D. Acta Mater 2006;54:2181.
- [47] Roters F, Eisenlohr P, Hantcherli L, Tjahjanto DD, Bieler T, Raabe D. Acta Mater 2010;58:1152.
- [48] Bulatov VV, Cai W. Computer simulation of dislocations. New York: Oxford University Press; 2006.
- [49] Kubin LP, Canova G, Condet M, Devincre B, Pontikis V, Brechet Y. Solid State Phenomena 1992;23–24:455.
- [50] Xiang Y, Cheng LT, Srolovitz DJ, Weinan E. Acta Mater 2003;51:5499.
- [51] Weygand D, Friedman LH, Van der Giessen E, Needleman A. Model Simul Mater Sci 2002;10:437.
- [52] Liu B, Raabe D, Eisenlohr P, Roters F, Arsenlis A, Hommes G. Acta Mater 2011;59:7125.
- [53] Madec R, Devincre B, Kubin LP, Hoc T, Rodney D. Science 2003;301:1879.
- [54] Bulatov VV, Hsiung LL, Tang M, Arsenlis A, Bartelt MC, Cai W, et al. Nature 2006;440:1174.
- [55] Liu B, Eisenlohr P, Roters F, Raabe D. Acta Mater 2012;60:5380.
- [56] Zbib HM, Rhee M, Hirth JP. Int J Mech Sci 1998;40:113.
- [57] Schwarz KW. J Appl Phys 1999;85:108.
- [58] Ghoniem NM, Tong SH, Sun LZ. Phys Rev B 2000;61:913.
- [59] Tang H, Schwarz KW, Espinosa HD. Phys Rev Lett 2008;100:185503.
- [60] Senger J, Weygand D, Gumbsch P, Kraft O. Scripta Mater 2008;58:587.
- [61] Devincre B, Hoc T, Kubin LP. Science 2008;320:1745.
- [62] Devincre B, Kubin LP, Hoc T. Scripta Mater 2006;54:741.
- [63] Wickham LK, Schwarz KW, Stolken JS. Phys Rev Lett 1999;83:4574.
- [64] Madec R, Devincre B, Kubin LP. Comput Mater Sci 2002;23:219.
- [65] Dupuy L, Fivel MC. Acta Mater 2002;50:4873.
- [66] Madec R, Kubin LP. In: Kitagawa H, Shibutani Y, editors. IUTAM symposium on mesoscopic dynamics of fracture process and materials strength, Osaka, Japan. Dordrecht: Kluwer Academic Publishers; 2004. p. 69–78.
- [67] Bulatov VV, Abraham FF, Kubin LP, Devincre B, Yip S. Nature 1998;39:669.
- [68] Raabe D. Philos Mag A 1998;77:751.
- [69] Madec R, Devincre B, Kubin LP. Scripta Mater 2002;47:689.
- [70] Motz C, Weygand D, Senger J, Gumbsch P. Acta Mater 2009;57:1744.
- [71] Senger J, Weygand D, Kraft O, Gumbsch P. Model Simul Mater Sci 2011;19:074004.
- [72] El-Awady JA, Wen M, Ghoniem NM. J Mech Phys Solids 2009;57:32.
- [73] Mordehai D, Clouet E, Fivel M, Verdier M. Philos Mag 2008;88:899.
- [74] Gao Y, Zhuang Z, Liu ZL, You XC, Zhao XC, Zhang ZH. Int J Plast 2011;27:1055.
- [75] Ayas C, Deshpande VS, Geers MGD. Int J Plast 2012;60:1626.
- [76] Monnet G, Naamane S, Devincre B. Acta Mater 2011;59:451.
- [77] Bako B, Weygand D, Samaras M, Hoffelner W, Zaiser M. Phys Rev B 2008;78:144104.
- [78] Yashiro K, Kurose F, Nakashima Y, Kubo K, Tomita Y, Zbib HM. Int J Plast 2006;22:713.
- [79] Rao SI, Parthasarathy TA, Dimidukz DM, Hazzlediney PM. Philos Mag 2004;84:3195.
- [80] Vattré A, Devincre B, Roos A. Intermetallics 2009;17:988.
- [81] Vattré A, Devincre B, Roos A. Acta Mater 2010;58:1938.
- [82] Huang MS, Zhao LG, Tong J. Int J Plast 2012;28:141.
- [83] Arsenlis A, Cai W, Tang M, Rhee M, Oppelstrup T, Hommes G, et al. Model Simul Mater Sci 2007;15:553.
- [84] Madec R, Devincre B, Kubin LP. In: Shibutani Y, Kitagawa H, editors. Mesoscopic dynamics in fracture process and strength of materials. Dordrecht: Kluwer Academic Publishers; 2003. p. 115–35.
- [85] Bacon DJ, Osetsky YN. Dislocations in Solids 2009;15:23.
- [86] Keralavarma SM, Cagin T, Arsenlis A, Benzerga AA. Phys Rev Lett 2012;109:265504.
- [87] Agudo Jácome L, Nörtershäuser P, Heyer J-K, Lahni A, Frenzel J, Dlouhy A, Somsen C, Eggeler G. Acta Mater 2013;61:2926.